Transfer Excitation Processes Observed in N^{3+}–He and O^{3+}–He Collisions at E_{lab} = 33 eV

Yoh Itoh*

Physics Laboratory, Faculty of Science, Josai University, Saitama 350-0295, Japan

(Received)

We measured the relative state-selective differential cross sections (DCSs) for one-electron capture reactions using a crossed-beam apparatus. The scattering angle θ_{lab} studied in the laboratory frame ranged from −3.0° to 22° and the laboratory collision energy E_{lab} was 33 eV. Only the transfer excitation processes, i.e., the electron capture reactions with the simultaneous excitation of the projectile, were observed. The DCSs were determined for the following reactions: N^{3+} ($1s^2$ $2s^2$ ^1S) + He ($1s^2$ ^1S) → N^{2+} ($1s^2$ $2s2p^2$ ^2D) + He^+ ($1s$ ^2S) + 10.3 eV, O^{3+} ($1s^2$ $2s^2$ $2p$ ^2P) + He ($1s^2$ ^1S) → O^{2+} ($1s^2$ $2s$ $2p^3$ ^3P) + He^+ ($1s$ ^2S) + 12.7 eV, and O^{3+} ($1s^2$ $2s^2$ $2p$ ^2P) + He ($1s^2$ ^1S) → O^{2+} ($1s^2$ $2s$ $2p^3$ ^3D) + He^+ ($1s$ ^2S) + 15.5 eV. In the N^{3+}–He system, the DCSs for the reaction are zero at the center-of-mass angle θ_{cm} = 0 and show a peak at a certain angle and a shoulder at a larger angle. In the O^{3+}–He system, the DCSs are again zero at θ_{cm} = 0. The capture process to the O^{2+} ($1s^2$ $2s$ $2p^3$ ^3P) state is mainly observed at smaller scattering angles, and the reaction to the O^{2+} ($1s^2$ $2s$ $2p^3$ ^3D) state becomes dominant with increasing scattering angle. A classical trajectory analysis within the two-state approximation based on the ab initio potentials for $(NHe)^{3+}$ revealed that the transfer excitation of a two-electron process takes place through a single crossing of the relevant potentials.

1. Introduction

The one-electron capture reactions in the collision of a multiply charged ion A^{q+} with a neutral atom B can be formally expressed as follows: $A^{q+} + B \rightarrow A^{(q-1)+} + B^+ + \Delta E$, where q is the charge state of the projectile ion and ΔE stands for the exothermicity. These reactions can be categorized into two types of processes.[1)] When a simple electron capture reaction occurs, only a single electron changes its orbital with no change in the configuration of the

other electrons in the projectile or target, which is called a type I process. In contrast, in a type II reaction, the electron capture reaction accompanies the excitation of the projectile or target, which is a typical two-electron process. Recently, the electron capture process with simultaneous excitation of the target, $H^+ + He \rightarrow H + He^{+*}$, has been studied in the high-energy region. For example, Schöffler et al.[2] measured the differential cross sections (DCSs) at a laboratory-frame collision energy E_{lab} ranging from 300 to 1200 keV. This two-electron process is studied as a typical example of a four-body problem.[3]

Among the type II reactions, the electron capture process with simultaneous excitation of the projectile is often called the "transfer excitation process" or "core-varying single-electron capture."[4] In 1979, Butler et al.[5] pointed out the theoretical importance of the transfer excitation process for collisions in N^{2+}–H and O^{2+}–H systems at thermal energies; however, there have been few systematic experimental studies in the low-energy region.[6]

To understand the reaction mechanism for the transfer excitation processes, Andersson et al.[7] suggested a model based on the configuration mixing of the Ar^{5+} ions created in the Ar^{6+}–He collisions in the energy range E_{lab} = 64–520 eV. Another mechanism was proposed by Gaboriaud et al.,[6] who studied the transfer excitation process by applying highly charged lithium-like ($1s^2$ 2s) ions and measured the state-selective DCSs for F^{6+} and Ne^{7+} with He and Ne collisions in the energy range E_{lab} = 3–10.5 keV. When they analyzed the data of these collisions, for example, $F^{+6}(1s^2\ 2s) + Ne \rightarrow F^{+5}(1s^2\ 2p\ 3s) + Ne^+$, they applied a model employing the idea of the nonresonant transfer excitation (NTE) process;[3] in other words, the excitation of the projectile originates from the interaction of the projectile electron with the target nucleus, whereas the target electron is transferred by its interaction with the projectile nucleus. Specifically, they treated the reaction as the following two-step

process: (i) the excitation of the projectile electron, 2s→2p, is caused by the Coulombic field induced by the target He^+ ion, and (ii) the electron transfer process occurs independent of the excitation process of the projectile. They pointed out that these two processes may occur successively at separate crossings or simultaneously at a single crossing.

This two-step model, however, does not always explain the data for reactions including lithium-like ions. By using lithium-like carbon ions, C^{3+} ($1s^2$ 2s), we previously reported the state-selective DCSs for the one-electron capture process in C^{3+}–He and C^{3+}–Ne systems at E_{lab} = 33 eV.[8] In the C^{3+}–He system, we observed only the simple one-electron capture process to the excited state of the projectile: C^{3+} ($1s^2$ 2s ^2S) + He ($1s^2$ ^1S) → C^{2+} ($1s^2$ 2s2p ^1P) + He^+ (1s ^2S) + 10.6 eV, whereas in the C^{3+}–Ne system, only the transfer excitation process C^{3+} ($1s^2$ 2s ^2S) + Ne ($2p^6$ ^1S) → C^{2+} ($1s^2$ $2p^2$ ^1D) + Ne^+ ($2p^5$ ^2P) + 8.2 eV was observed. If the two-step model can be applied to these collision systems, the transfer excitation process is expected to also occur in the C^{3+}–He system. The mechanism for the transfer excitation process in low-energy collisions has not yet been clarified.

In this paper, we report the transfer excitation processes observed in the N^{3+}–He and O^{3+}–He collision systems. The results of a classical trajectory analysis within the two-state approximation based on the ab initio potentials for $(NHe)^{3+}$ are shown, and a reaction mechanism at a single potential crossing is discussed.

2. Experimental Procedure

The experimental procedure was reported previously.[9] In brief, we produced N^{3+} and O^{3+} ions with an electron-beam ion source (EBIS). Energy- and momentum-selected ions were crossed with a supersonic target beam, and the energies of the scattered ions were

analyzed by using an electrostatic analyzer with a position-sensitive detection system.

The angular distribution was measured from the energy spectrum that was obtained by rotating the ion detector in 0.3° steps in the laboratory frame. The in-plane configuration was applied to precisely determine the collision kinematics, i.e., the ion detector was rotated in the plane of the crossed beams. The scattering angle θ_{lab} studied in the laboratory frame ranged from −3.0° to 22°.

The overall angular resolution in the laboratory frame was approximately ±0.8° at full width at half maximum. This corresponds to approximately ±0.06 rad in the center-of-mass frame at θ_{cm} = 0.25 rad for the N^{3+}–He system and ±0.07 rad at θ_{cm} = 0.35 rad in the O^{3+}–He system.

Collision energies were determined from the measured angular dependence of the elastically scattered ions. We calculated the angular dependence of the elastic scattering based on the kinematics, changing the collision energy as a parameter to reproduce the measured results. The collision energy of the present measurements was determined to be E_{lab} = 33 ± 1 eV.

The accumulation time was approximately 2–3 h at each angle. A peak-fitting program was used to integrate the ion counts under the peak area. The measured signals were then converted to the relative DCS, $d\sigma / d\Omega$, in the center-of-mass system in the standard manner. We assumed the same detection efficiency for the elastically scattered triply charged ions and for the doubly charged ions produced by the reactions when determining the DCSs for each channel.

3. Results and Discussion

3.1 Final-state analysis in N^{3+}–He

Figure 1(a) shows the measured energy spectra in a density plot obtained from θ_{lab} = 3.0–22°; namely, the energy spectra measured at different angles are plotted in a two-dimensional graph, and the intensities of the scattered ions are indicated by the darkness of the color. Noise counts were subtracted from the measured spectra, but no further data treatment was performed. The calculated positions for the elastically scattered N^{3+} ions at E_{lab} = 33 eV, which corresponds to the center-of-mass energy E_{cm} = 7.4 eV, are indicated by the curve labeled E in Fig. 1(a); the curve labeled 2 shows the calculated positions for reaction channel (2). A slight disagreement between curve E and the measured data is observed around θ_{lab} = 18°. We consider that this is caused mainly by the angular misalignment and the angular divergence of the beams, which were not taken into account in the present analysis. Examples of the individual spectra obtained at θ_{lab} = 5.1° and 9.0° are shown in Figs. 1(b) and 1(c), respectively. In these figures, the lines labeled 1–3 indicate the energy positions for the following reaction channels (1)–(3), respectively:

$$N^{3+}\,(1s^2\,2s^2\ {}^1S_g) + He\,(1s^2\ {}^1S_g)$$

$$\rightarrow N^{2+}\,(1s^2\,2s2p^2\ {}^2S_g) + He^{+}\,(1s\ {}^2S_g) + 6.6\ \text{eV}, \qquad (1)$$

$$\rightarrow N^{2+}\,(1s^2\,2s2p^2\ {}^2D_g) + He^{+}\,(1s\ {}^2S_g) + 10.3\ \text{eV}, \qquad (2)$$

$$\rightarrow N^{2+}\,(1s^2\,2s^2 2p\ {}^2P_u) + He^{+}\,(1s\ {}^2S_g) + 22.9\ \text{eV}. \qquad (3)$$

Reaction channels (1) and (2) are the transfer excitation process, whereas channel (3) is the simple electron capture process.

Radial coupling is considered to be responsible for the electron capture mechanism at low energies;[10] therefore, the symmetry of the quasi-molecular states generated from the initial states and the final states is conserved. The projectile N^{3+} ($1s^2\ 2s^2$) and the target He

($1s^2$) are both in the electronic state ^1S_g, where the parity symbols gerade (g) and ungerade (u) are used. The quasi-molecular state of the initial channel in the N^{3+}–He system is $^1\Sigma^+$; thus, we only considered the final channels with a symmetry of $^1\Sigma^+$.

We found that reaction channel (2) is the dominant process in this energy region that is, the electron is captured to the 2p state, and the 2s electron in the projectile is simultaneously excited to the 2p state. We thus conclude that the transfer excitation channel only opens in the N^{3+}–He system at E_{lab} = 33 eV.

Kamber et al.[11] measured the state-selective cross section in the N^{3+}–He system in the energy range E_{lab} = 6–15 keV. They revealed that reaction channel (2) dominates, and that reaction channel (1) is also significant. They showed that the cross section for reaction channel (3), a simple electron capture process, increases with increasing collision energies. They also examined the ratio of the cross section of the transfer excitation process to that of the total single-electron capture process and demonstrated that this ratio decreases with increasing collision energies.

The same trend, namely, the transfer excitation process becomes prominent at lower energies, was also found by Huber and Kahlert[12] when they studied the one-electron capture process in the Ne^{2+}–Xe system below E_{lab} = 1 keV. They attributed this trend to the longer collision time in the slower collisions; the longer interaction time would allow the rearrangement of the electron configuration of the quasi-molecular states created during the collisions. To the best of our knowledge, no state-selective measurement comparable to the present study has heretofore been made. However, the energy dependence of the cross section ratio reported by Kamber et al. and by Huber and Kahlert is considered to be consistent with the present results.

Ishii et al.[13] measured absolute integral cross sections for single- and double-electron capture processes in C^{q+}, N^{q+}, and O^{q+} (q = 2–6) on He systems in the energy region E_{lab} = q−1800q eV and analyzed the reaction channels by applying the classical over-barrier model (COBM)[14] as well as the multichannel Landau–Zener model.[15] Their analysis showed that the capture to N^{2+} ($1s^2$ $2s2p^2$ ^2D) dominates in the N^{3+}–He system; thus, our conclusion from the state-selective DCS measurement supports their interpretation.

Liu et al.[16] theoretically studied the state-selective integral cross sections for single- and double-electron capture processes in the N^{3+}–He collision system from E_{lab} = 0.1 eV to 15 keV. They applied the quantum-mechanical molecular-orbit close-coupling (QMOCC) method based on ab initio potentials. They concluded that the transfer excitation processes to N^{2+} ($1s^2$ $2s$ $2p^2$) states dominate in the energy region studied. We observed that only reaction channel (2) opens at E_{lab} = 33 eV, as shown above; however, their calculation indicates that the integral cross sections for reaction channels (1) and (2) are both about 5×10^{-16} cm^2 at E_{lab} = 30 eV. The reason for the discrepancy between the theoretical results and our measurements is presently not clear.

3.2 Final-state analysis in O^{3+}–He

The electronic state of the projectile O^{3+} ($1s^2 2s^2 2p$) is ^2P_u and that of the target He ($1s^2$) is ^1S_g. These two states yield $^2\Sigma^+$ and $^2\Pi$ states: thus, we consider the following reaction channels to analyze the measured spectra:

$$O^{3+}\,(1s^2\,2s^2\,2p\,{}^2P_u) + He\,(1s^2\,{}^1S_g)$$

$$\rightarrow O^{2+}\,(1s^2\,2s\,2p^3\,{}^1P_u) + He^+\,(1s\,{}^2S_g) + 4.3\ \text{eV}, \qquad (4)$$

$$\rightarrow O^{2+}\,(1s^2\,2s\,2p^3\,{}^1D_u) + He^+\,(1s\,{}^2S_g) + 7.2\ \text{eV}, \qquad (5)$$

$$\rightarrow O^{2+}(1s^2\ 2s\ 2p^3\ {}^3P_u) + He^+(1s\ {}^2S_g) + 12.7\ \text{eV}, \quad (6)$$

$$\rightarrow O^{2+}(1s^2\ 2s\ 2p^3\ {}^3D_u) + He^+(1s\ {}^2S_g) + 15.5\ \text{eV}, \quad (7)$$

$$\rightarrow O^{2+}(1s^2\ 2s^2\ 2p^2\ {}^1S_g) + He^+(1s\ {}^2S_g) + 25.0\ \text{eV}. \quad (8)$$

Reaction channels (4)–(7) are the transfer excitation processes and channel (8) is the simple electron capture process.

Figure 2(a) shows the measured energy spectra obtained in the range θ_{lab} = 3–18° in a density plot. The calculated positions for the elastically scattered O^{3+} ions at E_{lab} = 33 eV, which corresponds to E_{cm} = 6.7 eV, are indicated by the curve labeled E in Fig. 2(a). The curves labeled 6 and 7 indicate the calculated positions for reaction channels (6) and (7), respectively. The ion signals observed around channel 200 correspond to O^{2+} ions created by reactions. From θ_{lab} = 3° to about 7°, the peak positions of the spectra coincide with the calculated energy dependence for reaction channel (6). Upon increasing the scattering angle, the width of the spectra broadens, and the peak position of the spectra switches from the calculated position for reaction channel (6) to that for reaction channel (7).

Individual spectra obtained at θ_{lab} = 4.8° and 9.3° are shown in Figs. 2(b) and 2(c), respectively. Lines labeled 4–8 indicate the calculated energy positions for reaction channels (4)–(8), respectively. The ion intensities for each component were determined by applying a multipeak fitting program. The width of the fitting function for the product ions, O^{2+}, was taken to be 50% larger than that for the elastically scattered O^{3+} ions because the kinetic energies of the ions with different charge states were measured by an electrostatic energy analyzer. The results of the fitting procedure are shown in Figs. 2(b) and 2(c). In the energy spectra obtained at larger scattering angles, the product ions were found by analysis to be composed of the ions created by reaction channels (6) and (7). We thus conclude that only

reaction channel (6) opens for small scattering angles and that reaction channel (7) opens with increasing scattering angles. We again find that only the transfer excitation processes open for the one-electron capture reactions for O^{3+}–He collisions at E_{lab} = 33 eV.

Bangsgaard et al.[17] measured the ion spectra at θ_{lab} = 0º in the energy range E_{lab} = 250–1500 eV and determined the state-selective absolute cross sections. They showed that reaction channel (6) is the most significant and that the cross section for reaction channel (7) is of the same magnitude. In addition, they observed weaker ion signals for reaction channels (4) and (5). Thompson et al.[18] reported the energy spectrum of O^{2+} ions produced in O^{3+}–He collisions at E_{lab} = 12 keV. The trend of their results nearly coincides with those reported by Bangsgaard et al.; they also observed the simple electron capture process although it was unremarkable. The trends in these experimental results are similar to those observed in the N^{3+}–He collisions discussed in the previous subsection, namely, only a few transfer excitation channels open at lower energies, and a simple electron capture process starts to dominate with increasing collision energies.

Kamber et al.[19] measured integral cross sections for one-electron capture processes for E_{lab} = 0.3–1.2 keV and also studied the energy spectra of O^{2+} ions in the O^{3+}–He collision system at E_{lab} = 0.3 keV and for θ_{lab} = 0–4.1°. They observed no simple electron capture reactions and showed that reaction channels (6) and (7) dominate. When the scattering angle is θ_{lab} = 0º, the peak position of the spectrum coincides with that for reaction channel (6). As the scattering angle increases, the peak position of the spectra seems to shift slightly toward that for reaction channel (7). This behavior is consistent with our findings. Kamber et al. also observed reaction channels (4) and (5) and the transfer to the O^{2+} ($1s^2$ 2s $2p^3$ ^3S) state, and they showed that the DCSs for these channels decrease rapidly with increasing scattering

angle. We also carefully examined the ion signals around θ_{lab} = 0°; however, we could not distinguish O^{2+} ions created by the reactions from the noise counts.

Wu et al.[20] theoretically studied state-selective cross sections for single- and double-electron capture processes from E_{lab} = 0.18 eV to 18 keV by applying the QMOCC method based on ab initio potentials. They showed that transfer excitation processes dominate in this energy range. The integral cross section $\sigma(6)$ for reaction channel (6) is about 4.8×10^{-16} cm^2, whereas $\sigma(7)$ for reaction channel (7) is about 3.6×10^{-16} cm^2 at E_{lab} = 32 eV. The measured cross section ratio $\sigma(6)/\sigma(7)$ is discussed in Sect. 3.4. They also showed that the integral cross sections for reaction channels (4) and (5) are less than 10% of those of the dominant channels.

3.3 DCSs measured in N^{3+}–He

Figure 3 shows relative DCSs in the center-of-mass system for reaction channel (2) in the N^{3+}–He system and for the elastic scattering. Note that the DCS for the elastic scattering is divided by 2.5 to show the data on a comparable scale. Because we measured relative DCSs, the peak intensity for the reaction is normalized to unity. The error bars show the sum of the fluctuations of the ion signal and the imprecision of the peak-fitting procedure. The features of the DCS for the reaction are as follows: (i) the DCS is zero at the scattering angle θ_{cm} = 0 rad, (ii) it shows a prominent peak at θ_{cm} = 0.22 rad, and (iii) it has a small shoulder around θ_{cm} = 0.35 rad. These features are very similar to those observed in the C^{3+}–He collision system reported previously,[8] and the origin of the features is discussed in Sect. 3.6.

The DCS for elastic scattering shows almost no structure and decreases

monotonically with increasing scattering angle.

3.4 DCSs measured in O^{3+}–He system

Figure 4 shows the relative DCSs for both elastic and inelastic scattering in the O^{3+}–He collision system. The peak intensity for reaction channel (6) is normalized to unity. The DCS for the elastic scattering, which is multiplied by 1.5 in Fig. 4, shows almost no structure and decreases monotonically with increasing scattering angle. The DCS for reaction channel (6) is again zero at approximately $\theta_{cm} = 0$ rad and peaks at $\theta_{cm} = 0.30$ rad before decreasing almost monotonically at $\theta_{cm} = 0.40$–0.9 rad. The DCS for reaction channel (7) starts to appear at about $\theta_{cm} = 0.45$ rad and peaks near $\theta_{cm} = 0.7$ rad.

To compare the integral cross sections for reaction channels (6) and (7), we integrated the experimental DCSs multiplied by the geometrical factor sin θ_{cm} over the measured angular range in this study, i.e., $\theta_{cm} = 0.21$–0.90 rad for reaction channel (6) and $\theta_{cm} = 0.48$–0.99 rad for reaction channel (7). Because we measured only relative DCSs, we can only determine the cross section ratio $\sigma(6)/\sigma(7)$; we obtain $\sigma(6)/\sigma(7) = 1.8 \pm 0.5$, neglecting the contribution from the large angles of $\theta_{cm} > 1$ rad. The ratio predicted theoretically by Wu et al.[20] is 1.33. The error of our result is so large that we cannot determine the ratio clearly, but our result appears to be slightly larger than the theoretical value.

3.5 Final-state analysis based on reaction window

For a semiquantitative understanding of the state selectivity of the transfer excitation process observed in the N^{3+}–He collision system, we compare the measured exothermicity with the peak position of the calculated reaction windows. Because we found experimentally

that only reaction channel (2) opens, we applied the two-state approximation. Atomic units are used hereafter unless otherwise indicated.

The reaction window based on the Landau–Zener formula[21] and that based on the COBM model[14] are often used. To apply the Landau–Zener formula, the coupling matrix elements H_{12} must be determined; these are derived from the potential energy difference at the crossing point or are evaluated by using the empirical formula proposed by Olson and Salop[22] or by Kimura et al.[23] When we examine the energy difference of the theoretical potentials given by Liu et al.,[16] we find that the energy difference of the potential energies between 2Σ and 3Σ at the crossing point, which corresponds to reaction channel (2), is very small; thus, we cannot evaluate H_{12}. We cannot decide an appropriate way to determine the coupling matrix elements; therefore, we only examine the reaction window based on the ECOB model. In the ECOB model, the exothermicity for the reactions is $(q–1)/R_c$. The capture distance R_c at which the reaction can occur is given by $R_c = (2\sqrt{q}+1)/I_t$, where I_t is the ionization energy of the target. The width of the reaction window is calculated by using Eq. (20) from Ref. 14. The reaction window for the O^{3+}–He system is also calculated in the same manner and almost coincides with that for the N^{3+}–He collision system. The width depends on the velocities of the projectiles, and the velocities of the N^{3+} and O^{3+} ions are almost the same at the same collision energy.

The calculated reaction window is shown in Fig. 5. The peak value in the reaction window is normalized to unity. The exothermicities for reaction channels (2), (6), and (7) are indicated by arrows in Fig. 5. The dominant reaction channels (2) and (6) are located within the reaction window; therefore, the state selectivity for the transfer excitation is understood to be well explained by the reaction window based on the COBM model.

3.6 Origin of structures in DCSs

When we study an electron capture reaction that occurs near the crossing point of the relevant potentials, we consider two pathways: the reaction that occurs in the incoming part of the trajectory at the first crossing, and the reaction that occurs in the outgoing part of the trajectory at the second crossing. Taking into account these trajectories within the two-state approximation, we previously analyzed the structure in the DCSs for the simple electron capture process in the C^{3+}–He system.[8] The results are as follows: (i) the prominent peak is due to the inelastic rainbow[24] and (ii) the broad hump is caused mainly by the DCS due to the reaction that occurred in the incoming part of the trajectory.

As shown in Sects. 3.3 and 3.4, only reaction channel (2) opens in the N^{3+}–He collision system, and the features of the DCSs are very similar to those in the C^{3+}–He collision system. Therefore, we expect to gain insights into the origin of the features for the transfer excitation process by applying a similar analysis. We thus calculated the deflection function; namely, the deflection angle Θ as a function of impact parameter b, for comparison with the measured results. The following model potentials were used for the calculation. We used the theoretical potentials reported by Liu et al.[16] by reading the potential data from Fig. 1 of their publication, then we set up the following Morse-type potential for the initial channel:

$$V_{\text{in}}(r) = 0.0159\{\exp[1.825(4.40 - r)] - 2\exp[1.825(4.40 - r)]\} \quad . \qquad (9)$$

Only the Coulomb repulsive potential and the exothermicity are considered for the reaction channel:

$$V_{\text{out}}(r) = 2/r - 0.3798 \, . \qquad (10)$$

These model and theoretical potentials are compared in Fig. 6, and the calculated deflection function is shown in Fig. 7.

The classical DCS for reactions is

$$\frac{d\sigma}{d\Omega} = \sum_{\mathrm{j}} \frac{b_{\mathrm{j}}}{\sin\theta_{\mathrm{cm}}} \left| \frac{d\Theta}{db_{\mathrm{j}}} \right|^{-1} \cdot P(b_{\mathrm{j}}) \ , \qquad (11)$$

where b_{j} is the possible impact parameter that leads to the same scattering θ_{cm} and $P(b)$ is the transition probability for the reaction. The scattering angle in the center-of-mass system is generally given by $\theta_{\mathrm{cm}} = |\Theta|$.

In Fig. 7, we see that the deflection function relevant to the outgoing part of the trajectory has a minimum at b = 4.6 a.u.; this impact parameter corresponds to the scattering angle θ_{cm} = 0.153 rad, which is the smallest scattering angle calculated. This trend in the deflection function explains the experimental results: the measured DCSs are zero around θ_{cm} = 0 rad. At the minimum angle, $d\Theta/db$ becomes zero; thus, the classical DCS diverges. This is the origin of the inelastic rainbow structure proposed by Olson and Kimura[24] and corresponds to the prominent peak observed in the DCSs at θ_{cm} = 0.22 rad; the measured angle is slightly larger than the calculated minimum angle θ_{cm} = 0.153 rad.

We also see that the smallest scattering angle relevant to the incoming part of the trajectory is 0.364 rad at b = 5.51 a.u. in Fig. 7. The reaction in the incoming part of the trajectory contributes to the DCSs when the scattering angle is larger than this angle. The measured DCS shown in Fig. 3 has a shoulder structure around θ_{cm} = 0.35 rad, which is very close to the angle of 0.364 rad at b = 5.51 a.u. Thus, the observed structure is attributed to the contribution of the DCS in the incoming part of the trajectory.

The calculated positions for the peak and shoulder of the DCSs differ slightly from

the measured positions; however, the present analysis, which accounts for the single potential crossing, can convincingly explain the observed features of the DCSs in the N^{3+}–He system. Thus, we conclude that the transfer excitation process, a typical two-electron process, in the N^{3+}–He system occurs at a single-crossing point of the relevant potentials.

Because two reaction channels open in the O^{3+}–He system, we cannot apply the simple classical trajectory analysis to the system within the two-state approximation. As we showed in Sect. 3.2, the quasi-molecular states formed during the collision in the O^{3+}–He system are $^2\Sigma^+$ and $^2\Pi$. From the symmetry consideration in the radial coupling mechanism, we know that both states correlate with reaction channel (6), while reaction channel (7) corresponds only to the $^2\Pi$ states.

Wu et al.[20] reported the locations of strong avoided crossings in the ab initio potentials and suggested the importance for one-electron capture reactions. They showed that the crossings responsible for reaction channel (6) are located around the internuclear distances of 2.40 and 4.40 a.u. for the $^2\Sigma^+$ states. In the $^2\Pi$ states, the avoided crossings responsible for reaction channel (6) are located around the internuclear distances of 2.40 and 4.39 a.u., and the avoided crossing for reaction channel (7) is located at around 2.70 a.u.

The crossing points at the internuclear distance of 2.40 a.u. in the $^2\Sigma^+$ and $^2\Pi$ states are located about 6.6 eV above the initial channel; it is hardly possible to access these crossing points with the present collision energy, E_{cm} = 6.7 eV. Thus, the two-state approximation can be applied for reaction channel (6) owing to the potential crossing in the $^2\Sigma^+$ states.

As no strong attractive potentials are seen in both the $^2\Sigma^+$ and $^2\Pi$ states, the value of the impact parameter b that is necessary to reach the crossing point is nearly the same or smaller than the crossing radius. Consequently, the collisions with the impact parameter between 2.70

and 4.40 a.u. only correlate with reaction channel (6) thus, the idea of a two-state approximation can be applied again under these conditions. The collisions with the impact parameter smaller than 2.70 a.u. are considered to correlate with both reaction channels (6) and (7) thus, a detailed analysis is required for such conditions.

These different impact parameter dependences for the reaction channels can be used to explain the measured results; only reaction channel (6) is observed at smaller scattering angles. The overall angular dependence of the DCS for reaction channel (6) seems to be similar to that for reaction (2) in the N^{3+}–He system; therefore, we expect the origin of the peak in the DCS for reaction channel (6) to be due to the inelastic rainbow. We tentatively conclude that the two-electron process in the O^{3+}–He collision system also takes place through a single crossing of the relevant potentials.

The exothermicity in reaction channel (7) is larger than that in reaction channel (6); therefore, the stronger Coulomb repulsion force after the reaction is attributed to the larger scattering angle observed for reaction channel (7).

3.7 Comparison of reaction probabilities in N^{3+}–He and O^{3+}–He systems

We define the reaction probability $P(\theta_{cm})$ as the ratio of the measured inelastic DCS to the sum of the measured elastic and inelastic DCSs at the same scattering angle θ_{cm}. One must note that the impact parameters that lead to the same scattering angle in the elastic and inelastic scatterings are generally different, especially in low-energy collisions. Bearing in mind that $P(\theta_{cm})$ cannot always directly reflect the impact parameter dependence of the transition probability $P(b)$, we evaluated the reaction probabilities to obtain information on the transition probability $P(b)$ from the measurements. The results are shown in Fig. 8.

We see in Fig. 8 that $P(\theta_{cm})$ in the N^{3+}–He system differs considerably from that in the O^{3+}–He system. $P(\theta_{cm})$ in the N^{3+}–He system increases monotonically and shows no structure in the range θ_{cm} = 0.15–0.35 rad, whereas in the O^{3+}–He system, $P(\theta_{cm})$ shows a prominent peak near θ_{cm} = 0.35 rad.

In the N^{3+}–He system, the peak position of the DCS for reaction channel (2) shown in Fig. 3 is about 0.22 rad. As shown in Fig. 7, the DCSs in the range θ_{cm} = 0.15–0.35 rad are mainly determined by the reaction that occurred in the outgoing part of the trajectory, and the relevant values of the impact parameter are about b = 3.5–5.5 a.u. If the transition probabilities are large for these values of the impact parameter, some structure in $P(\theta_{cm})$ is expected to appear because the classical DCS itself diverges at b = 4.6 a.u. The absence of a structure in $P(\theta_{cm})$ for the N^{3+}–He system suggests that $P(b)$ is not large in this range of the impact parameter.

In the O^{3+}–He system, $P(\theta_{cm})$ shows a prominent peak near θ_{cm} = 0.35 rad and broad structure at larger scattering angles due to the opening of reaction channel (7). The peak position in $P(\theta_{cm})$ coincides with that of the DCS for reaction channel (6) shown in Fig. 4. The impact parameter corresponding to the inelastic rainbow scattering is often slightly smaller than the crossing radius. The internuclear distance of the potential crossing relevant to reaction channel (6) was shown to be about 4.4 a.u. by Wu et al.,[20] and the origin of the peak in the DCS for reaction channel (6) is tentatively assigned to the inelastic rainbow; thus, $P(b)$ for this channel should be large when the impact parameter is around b = 4 a.u.

As we discussed in Sect. 3.6, the avoided crossings in both the $^2\Sigma^+$ and $^2\Pi$ states contribute to reaction channel (6). In Table II of Ref. 20, the energy difference between the relevant potentials for the $^2\Pi$ states at the crossing radius of 4.39 a.u. is shown to be

approximately twofold smaller than that for the $^2\Sigma^+$ states at 4.40 a.u.; therefore, the reaction path through the avoided crossing in the $^2\Pi$ states seems to be more favorable than that through the crossing in the $^2\Sigma^+$ states. It should be pointed out that the numerical value for the energy difference ΔU given in Table II of Ref. 20 is considered to be in atomic units and not in eV.[25)]

4. Summary

We measured the state-selective DCSs in the N^{3+}–He and O^{3+}–He collision systems at E_{lab} = 33 eV. Only the transfer excitation processes to the N^{2+} ($1s^2$ $2s2p^2$ ^2D) state in the N^{3+}–He system and the O^{2+} ($1s^2$ $2s$ $2p^3$ ^3P) and O^{2+} ($1s^2$ $2s$ $2p^3$ ^3D) states were observed. We analyzed the distributions of the final channels on the basis of the reaction window by applying the COBM model. The reaction window convincingly explained the exothermicities favored for the main transfer excitation processes. A classical trajectory analysis within the two-state approximation based on the ab initio potentials for $(NHe)^{3+}$ revealed that the transfer excitation of the two-electron process takes place through a single crossing of the potentials relevant to the reaction. The measured peak in the DCS is attributed to the inelastic rainbow, and the shoulder structure mainly originates from the contribution of the reaction that occurs in the incoming part of the trajectory. The origin of the structure in the DCSs observed in the O^{3+}–He collision system is also tentatively assigned to be the same as that in the N^{3+}–He system.

Acknowledgments

This paper is dedicated to the late Dr. Kazumasa Ohtsuki, who provided me with his unpublished theoretical potentials. This work was partly supported by a Grant-in-Aid for Scientific Research (17540373).

* yitoh @josai.ac.jp

References

1) S. E. Butler and A. Dalgarno, Astrophys. J. **241**, 838 (1980).

2) M. S. Schöffler, H.-K. Kim, O. Chuluunbaatar, S. Houamer, A. G. Galstyan, J. N. Titze, T. Jahnke, L. Ph. H. Schmidt, H. Schmidt-Böcking, R. Dörner, Yu. V. Popov, and A. A. Bulychev, Phys. Rev. A **89**, 032707 (2014).

3) D. Belkić, I. Mančev, and J. Hanssen, Rev. Mod. Phys. **80**, 249 (2008).

4) J. Schweinzer and H. Winter, J. Phys. B **23**, 3899 (1990).

5) S. E. Butler, C. F. Bender, and A. Dalgarno, Astrophys. J. **230**, L59 (1979).

6) M. N. Gaboriaud, M. Barat, P. Roncin, and V. Sidis, J. Phys. B **27**, 4595 (1994).

7) L. R. Andersson, H. Cederquist, A. Bárány, L. Liljeby, C. Biedermann, J. C. Levin, N. Keller, S. B. Elston, J. P. Gibbons, K. Kimura, and I. A. Sellin, Phys. Rev. A **43**, 4075 (1991).

8) Y. Itoh, J. Phys. Soc. Jpn. **84**, 064301 (2015).

9) Y. Itoh, J. Phys. B **44**, 175202 (2011) [Erratum **44**, 239601 (2011)].

10) M. Gargaud, J. Hanssen, R. McCarroll, and P. Valiron, J. Phys. B **14**, 2259 (1981).

11) E. Y. Kamber, K. Akgüngör, C. Leather, and A. G. Brenton, Phys. Rev. A **54**, 1452 (1996).

12) B. A. Huber and H.-J. Kahlert, J. Phys. B **17**, L69 (1984).

13) K. Ishii, A. Itoh, and K. Okuno, Phys. Rev. A **70**, 042716 (2004).

14) A. Niehaus, J. Phys. B **19**, 2925 (1986).

15) A. Salop and R. E. Olson, Phys. Rev. A **13**, 1312 (1976).

16) X. J. Liu, J. G. Wang, Y. Z. Qu, and R. J. Buenker, Phys. Rev. A **84**, 042706 (2011).

17) J. P. Bangsgaard, P. Hvelplund, J. O. P. Pedersen, L. R. Andersson, and A. Bárány, Phys. Scr. T **28**, 91 (1989).

18) W. R. Thompson, D. Burns, D. Voulot, R. W. McCullough, J. Geddes, and H. B. Gilbody, Phys. Scr. T **80**, 362 (1999).

19) E. Y. Kamber, O. Abu-Haija, and J. A. Wardwell, Phys. Rev. A **77**, 012701 (2008).

20) Y. Wu, Y. Y. Qi, S. Y. Zou, J. G. Wang, Y. Li, R. J. Buenker, and P. C. Stancil, Phys. Rev. A **79**, 062711 (2009).

21) K. Taulbjerg, J. Phys. B **19**, L367 (1986).

22) R. E. Olson and A. Salop, Phys. Rev. A **14**, 579 (1976).

23) M. Kimura, T. Iwai, Y. Kaneko, N. Kobayashi, A. Matsumoto, S. Ohtani, K. Okuno, S. Takagi, and H. Tawara, J. Phys. Soc. Jpn. **53**, 2224 (1984).

24) R. E. Olson and M. Kimura, J. Phys. B **15**, 4231 (1982).

25) K. Ohtsuki, private communication.

Figures

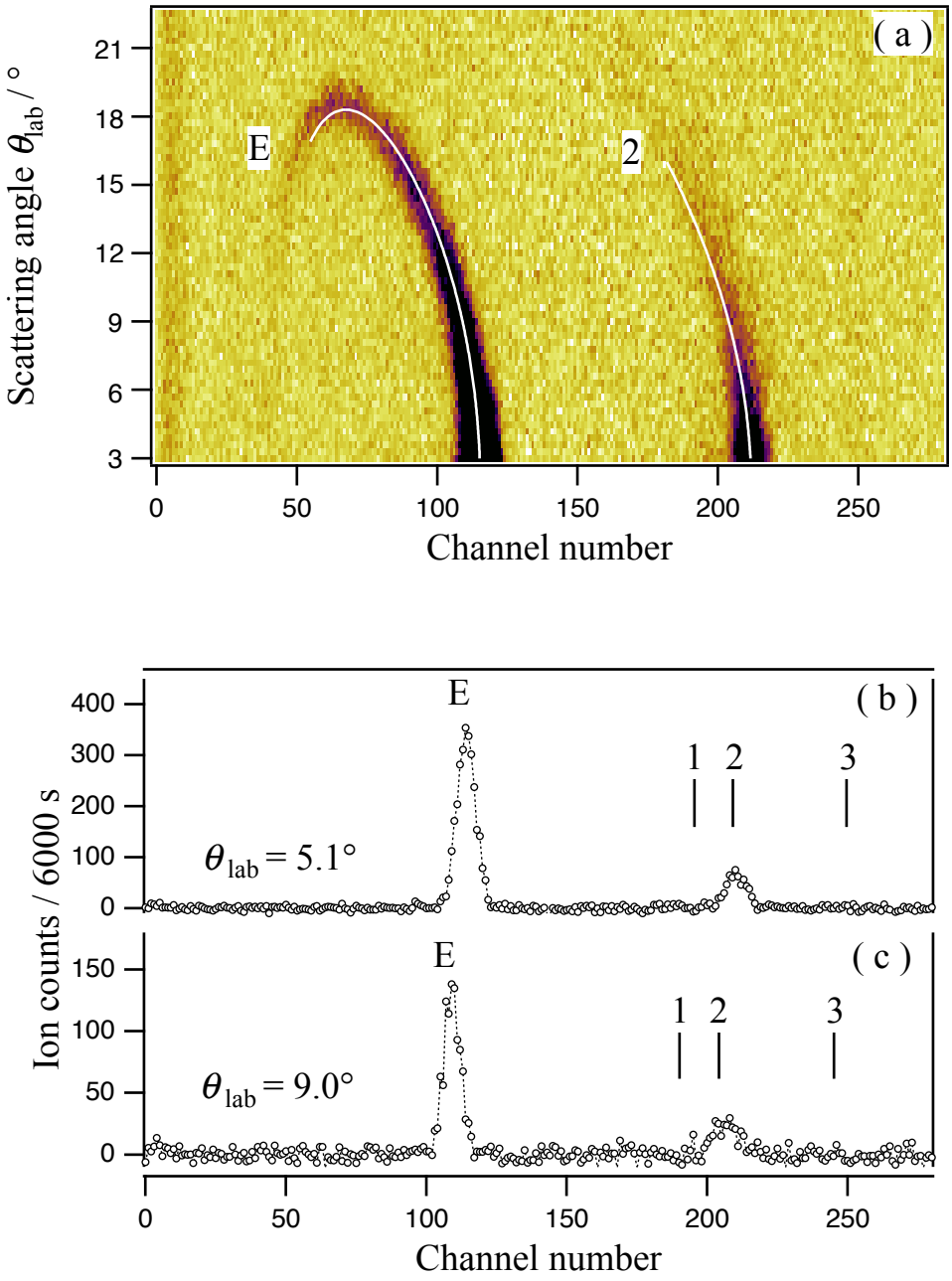

Fig. 1. (Color online) (a) Energy spectra of scattered ions in the N^{3+}–He collision system at E_{lab} = 33 eV. Measured spectra are shown in a density plot (see text). The channel number corresponds to the kinetic energy of the ions; the energy increment is approximately 0.103q eV. Curve E shows the calculated position for the elastically scattered ions. Curve 2 shows the calculated positions for reaction channel 2: N^{3+} ($1s^2$ $2s^2$ ^1S) + He ($1s^2$ ^1S)→ N^{2+} ($1s^2$

$2s2p^2\ ^2D$) + He^+ ($1s\ ^2S$) + 10.3 eV. (b) Individual energy spectrum obtained at θ_{lab} = 5.1°. Lines 1–3 show the calculated energy positions for reaction channels (1)–(3), respectively. (c) Individual energy spectrum obtained at θ_{lab} = 9.0°.

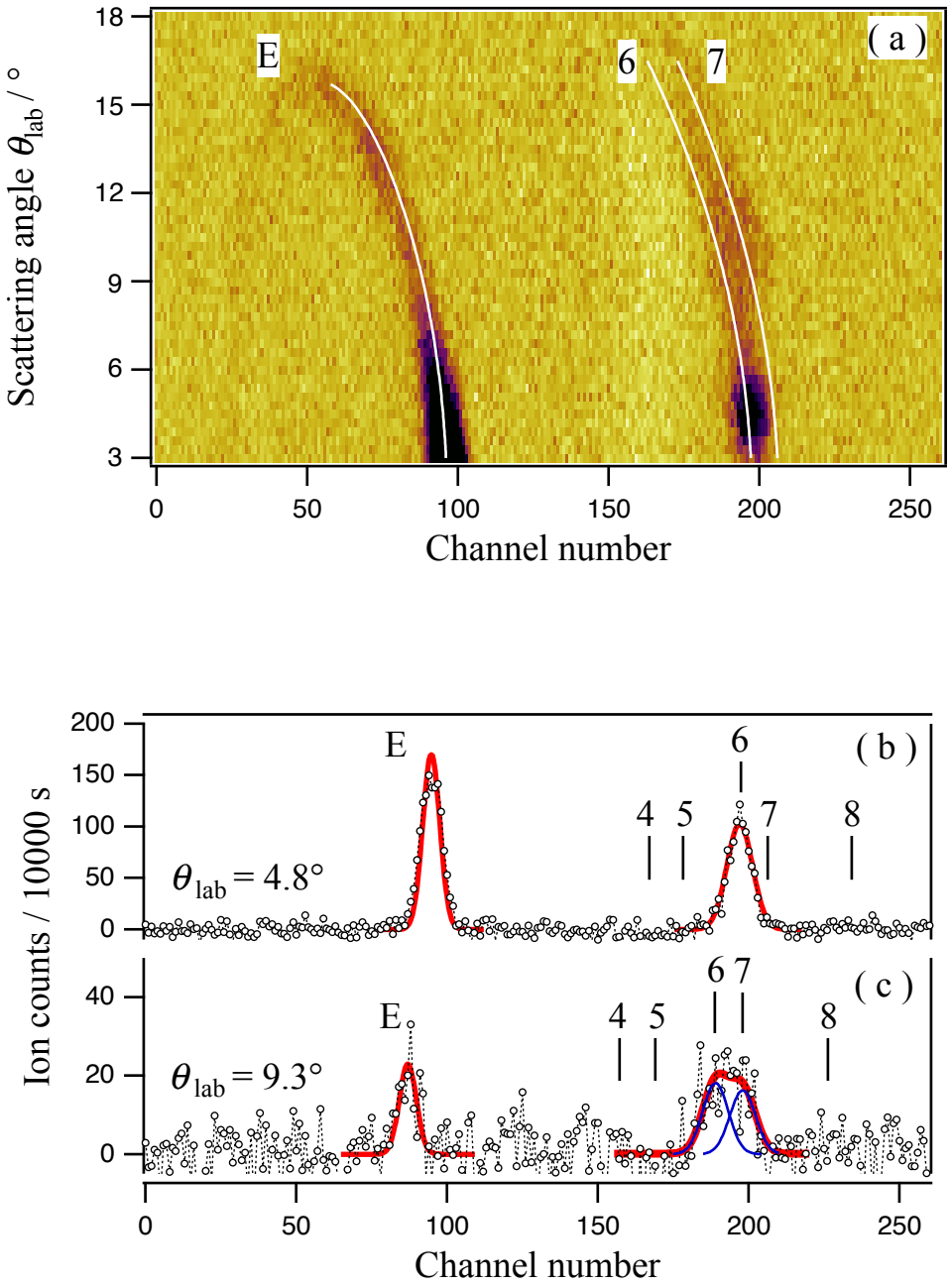

Fig. 2. (Color online) (a) Energy spectra of scattered ions in the O^{3+}–He collision system at E_{lab} = 33 eV. Measured spectra are shown in a density plot. Curve E shows the calculated position for the elastically scattered ions. Curves 6 and 7 respectively show the calculated positions for reaction channels (6): O^{3+} ($1s^2$ $2s^2$ $2p\ ^2P$) + He ($1s^2\ ^1S$) → O^{2+} ($1s^2$ $2s$ $2p^3\ ^3P$) + He^+ ($1s\ ^2S$) + 12.7 eV, and (7): O^{3+} ($1s^2$ $2s^2$ $2p\ ^2P$) + He ($1s^2\ ^1S$) → O^{2+} ($1s^2$ $2s$ $2p^3\ ^3D$) + He^+ ($1s\ ^2S$) + 15.5 eV. Individual energy spectrum obtained at θ_{lab} = 4.8° (b) and that obtained at

θ_{lab} = 9.3° (c). Results of the peak-fitting procedure are shown by solid curves in (b) and (c).

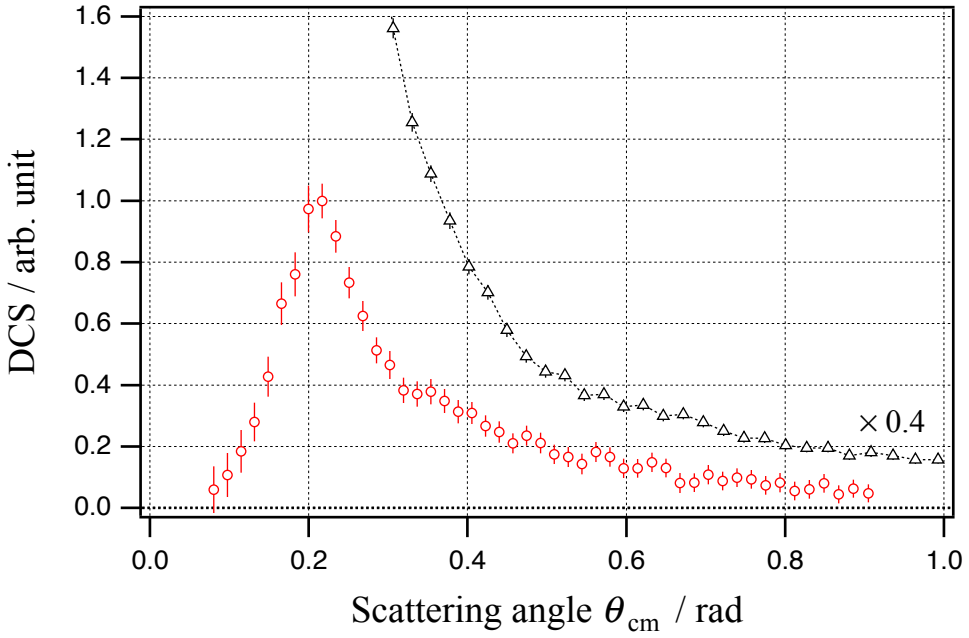

Fig. 3. (Color online) Relative DCSs in the center-of-mass system in the N^{3+}–He collisions at E_{cm} = 7.4 eV; open triangles correspond to elastic scattering and open circles correspond to the reaction N^{3+} ($1s^2\ 2s^2\ ^1S$) + He ($1s^2\ ^1S$)→ N^{2+} ($1s^2\ 2s2p^2\ ^2D$) + He^+ ($1s\ ^2S$) + 10.3 eV. The DCS for the elastic scattering is divided by 2.5.

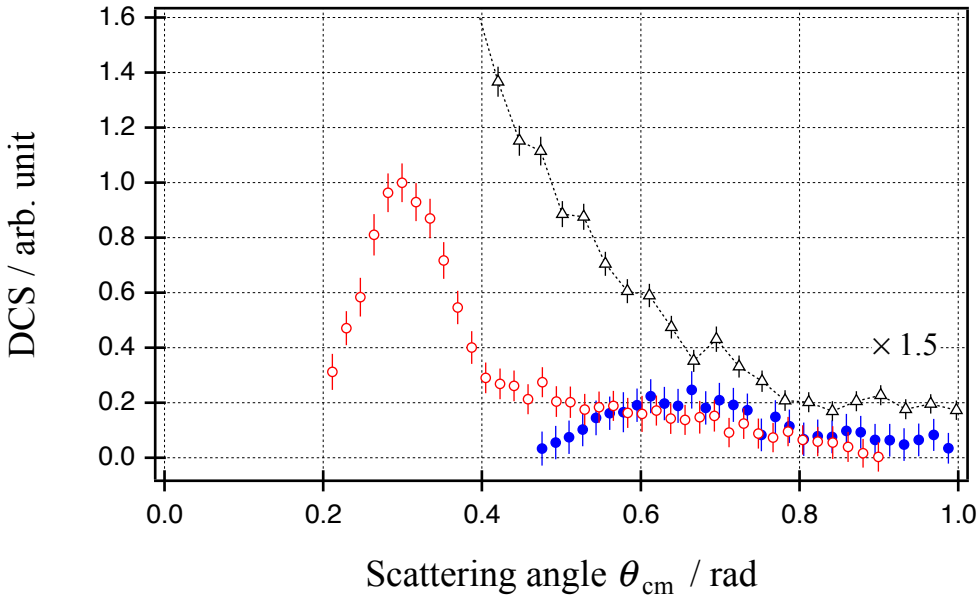

Fig. 4. (Color online) Relative DCSs in the center-of-mass system in the O^{3+}–He collisions at E_{cm} = 6.7 eV; open triangles correspond to elastic scattering, open circles correspond to the reaction O^{3+} ($1s^2\ 2s^2\ 2p\ ^2P$) + He ($1s^2\ ^1S$) → O^{2+} ($1s^2\ 2s\ 2p^3\ ^3P$) + He^+ ($1s\ ^2S$) + 12.7 eV, and solid circles correspond to O^{3+} ($1s^2\ 2s^2\ 2p\ ^2P$) + He ($1s^2\ ^1S$) → O^{2+} ($1s^2\ 2s\ 2p^3\ ^3D$) + He^+ ($1s\ ^2S$) + 15.5 eV. The DCS for the elastic scattering is multiplied by 1.5.

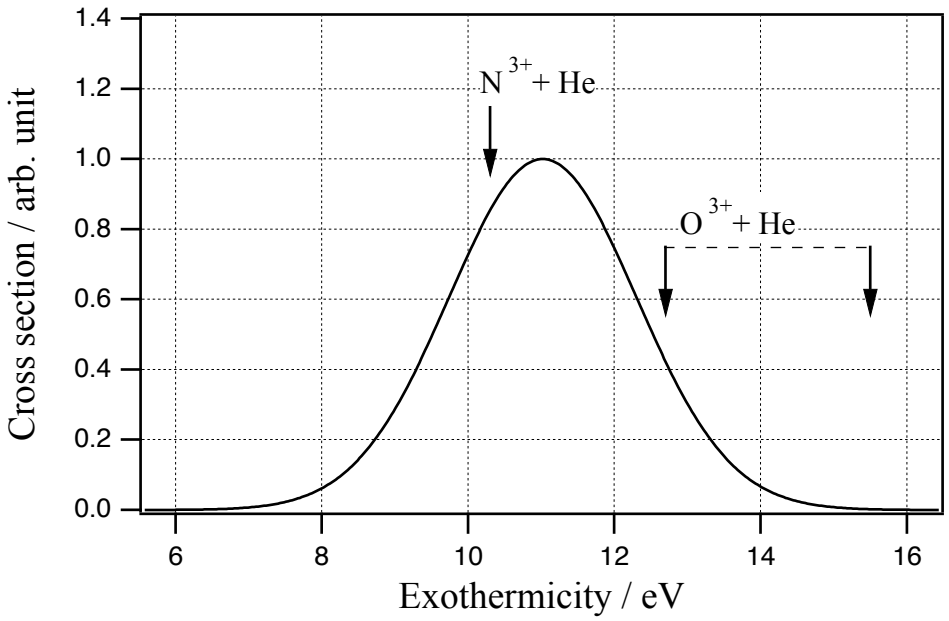

Fig. 5. Reaction window based on the COBM model at E_{lab} = 33 eV for the N^{3+}–He collision system. The arrows show the observed exothermicities in the N^{3+}–He and O^{3+}–He systems.

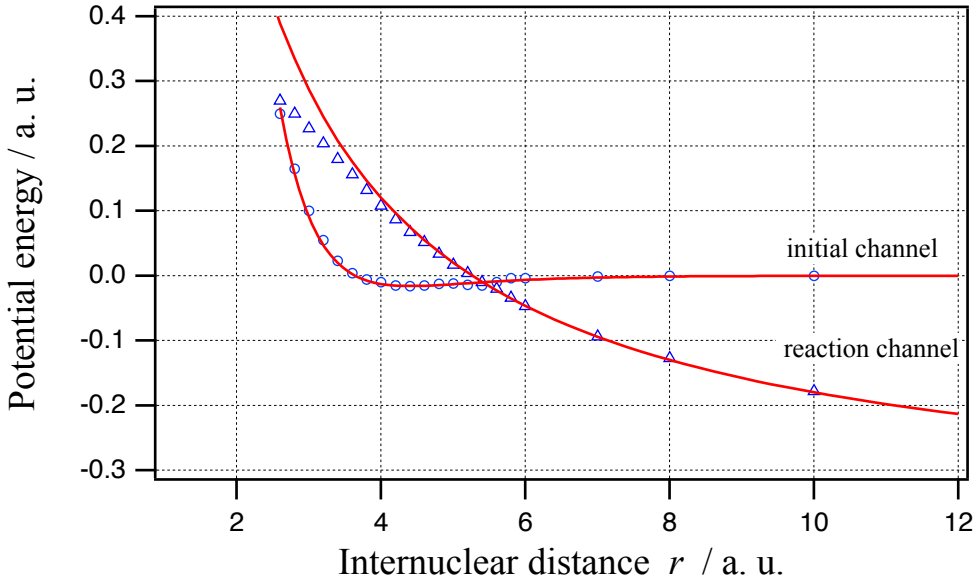

Fig. 6. (Color online) Curves show model potentials used to calculate the deflection function in the N^{3+}–He collision system. Symbols show ab initio potential energies reported by Liu et al.[16)]

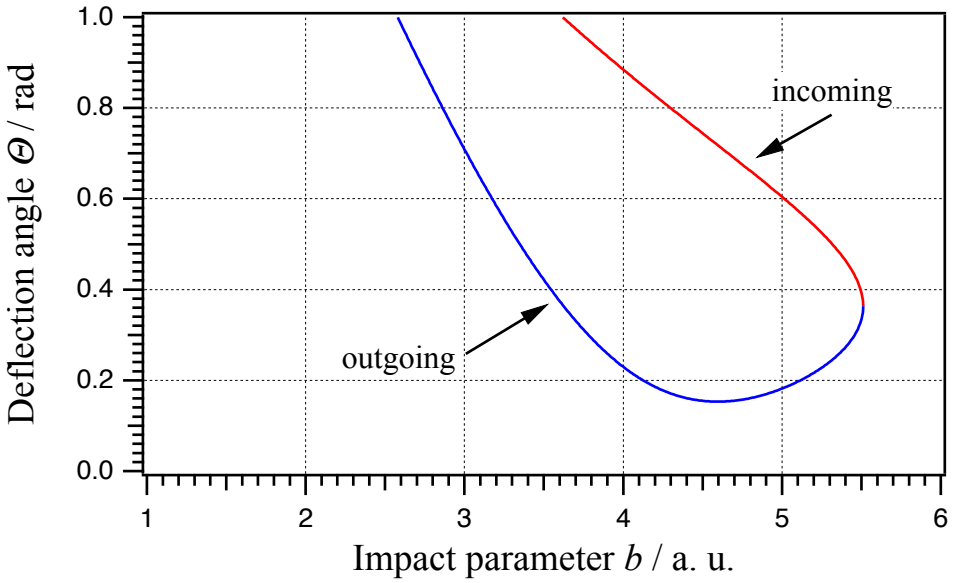

Fig. 7. (Color online) Deflection function for one-electron capture reaction (2) in the N^{3+}–He collision system at E_{lab} =33 eV. The upper part of the curve corresponds to the reaction that occurs in the incoming part of the trajectory, and the lower half of the curve corresponds to the reaction that occurs in the outgoing part of the trajectory.

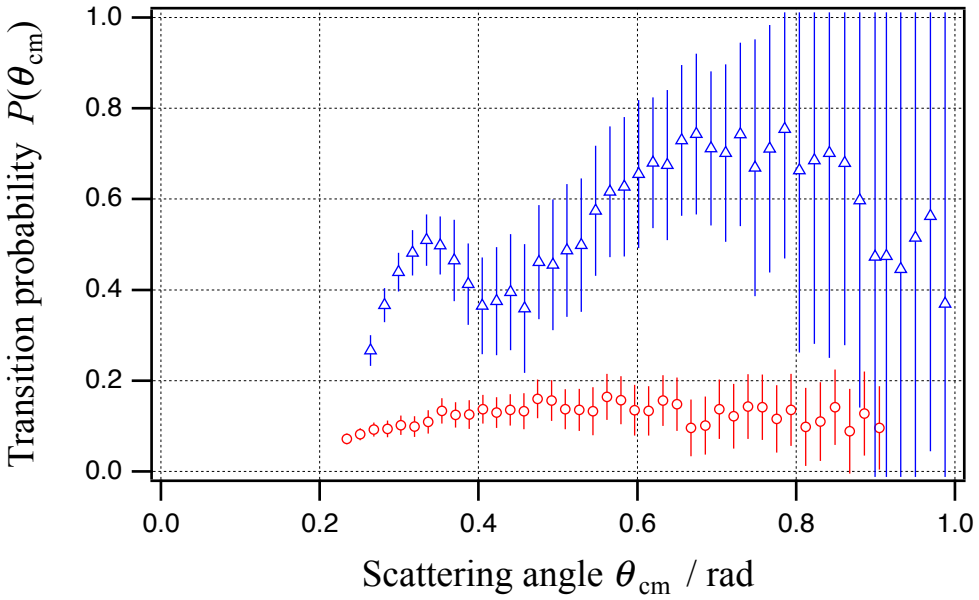

Fig. 8. (Color online) Comparison of reaction probabilities (see text) at E_{lab} =33 eV; open circles are for the N^{3+}–He system and open triangles are for the O^{3+}–He system.